Pergamon

Int. J. Heat Mass Transfer. Vol. 40, No. 5, pp. 1131–1143, 1997
Copyright © 1996 Elsevier Science Ltd
Printed in Great Britain. All rights reserved
0017-9310/97 $17.00+0.00

PII: S0017-9310(96)00124-X

Laser heating process and experimental validation

B. S. YILBAS
Mechanical Engineering Department, KFUPM, Dhahran, Saudi Arabia

(*Received* 30 *August* 1995 *and in final form* 2 *April* 1996)

Abstract—Laser machining of engineering materials requires deep investigation into the laser–workpiece interaction mechanism, which is generally complicated and depends on the laser and workpiece properties. The present study examines the heat transfer mechanism, including conduction, phase change and convection processes taking place during Nd YAG laser irradiation of steel workpieces. Gaussian profile is considered for the spatial distribution of the laser output power intensity, while a time-dependent profile resembling the actual laser output pulse is introduced in computation. The thermal properties of the substance is considered as temperature dependent. Mass removal from the laser irradiated spot is modeled considering momentum and continuity equations. To validate the theoretical predictions, experimental measurements of surface temperature and evaporating surface velocities are carried out. Optical method and streak photography techniques are employed for this purpose. It is found that surface temperatures and evaporating front velocities are in good agreement with the experimental results. Copyright © 1996 Elsevier Science Ltd.

INTRODUCTION

Laser material processing has made significant headway into the well-established area of the sheet metal industry. This is due to its low operational cost and high precision. When a high intensity laser is directed onto a metal surface, heating, melting and evaporation of the substance occur, therefore, conduction, phase change and convection processes result. To enhance understanding of laser–workpiece interaction mechanism, the study into laser-induced heating and subsequent material removal, initiating the laser machining process, is necessary.

Although a number of heat transfer models for laser material processing have previously been reported [1–4], only a few [3, 4] compare the simulation results directly with experiments. The heat transfer model presented previously for laser machining considered the material as remaining in either the solid or the liquid phase, depending on the local temperature [2]. Analysis of heat conduction in deep penetration welding with a time-modulated laser beam output was studied by Simon *et al.* [5] using a cylinder-type heat source. They showed that the temperature distribution was highly depended on the modulation frequency. However, in an actual case, the spatial distribution of laser output power intensity is Gaussian in nature and the results predicted from these studies are not consistent with the experimental findings. Diniz Neto and Lima [6] computed the temperature profiles inside the substance subjected to high intensity and short pulse length laser irradiation using three-dimensional heat conduction equation. The applicability of the model developed to metals heated by a pulsed Nd YAG laser was discussed. However, this study was limited for conduction-only process, i.e. mass removal process due to surface evaporation was excluded. In order to describe the complete physical phenomena occurring during high intensity laser beam interaction with the substance, the effects of phase change must be included in the mathematical model. This case was considered by Blackwell [7]. He investigated the material removal process, initiated by a high power laser beam source, analytically by calculating the temperature profile in a semi-infinite body with an exponential decaying (spatially) source. He concluded that the maximum temperature lay below the surface and this depended on the Biot and Fourier numbers. The phase change process during laser–workpiece interaction was introduced by Duley [8] and used the speed of evaporation front based on the steady-state surface conditions, however, the same expression was also derived analytically in the previous study [9]. On the other hand, Yilbas and Sahin [10] carried out analytical study on high power laser heating process, assuming a constant surface evaporation rate. However, this assumption gives limited accuracy as compared to the actual case, since the surface evaporation rate is the function of the rise of the surface temperature.

The present study was conducted to determine the temporal and spatial distribution of temperature and evaporating surface velocities due to Nd YAG laser irradiation of steel workpiece. In the analysis, spatial distribution of laser power intensity is considered as a Gaussian while a time-dependent profile resembling the actual laser pulse is employed. The thermal properties of the substance are considered as tem-

NOMENCLATURE

A_e	surface area of east face of mesh
I_0	peak power intensity
C_p	specific heat constant at constant pressure
k	thermal conductivity
K_B	Boltzmann's constant
L	latent heat of evaporation
m	atomic mass
P	pressure
P^*	guessed pressure
r	radial distance
R	radius to $1/e$ point of Gaussian
R_f	surface reflectivity
s	distance normal to liquid surface
t	time
T	temperature
u^*	calculated velocity corresponding to the guessed pressure
v	specific volume
V	velocity
z	axial distance.

Greek symbols

α	thermal diffusivity
γ	specific heat ratio
ρ	density.

Subscripts

c	critical
i	at time $t = 0$
l	liquid state
N	on radial mesh line N
M	on axial mesh line M
0	reference state
r	radial
s	surface (in normal direction)
v	evaporation
z	axial
Δ	increment.

perature dependent. Mass removal from the irradiated spot is taken into account considering momentum and continuity equations. The study is extended to include the experimental measurements of surface temperature and evaporated surface velocities. To accomplish the measurements, an optical method is used to measure the surface temperature of the irradiated spot, while a streak photography technique is introduced for the evaporated surface velocity measurements.

MATHEMATICAL MODELING AND NUMERICAL APPROACH

Absorption of light in metals leads initially to an increase in the temperature of the free electron gas which then transfers energy to the lattice by collision [11]. The latter process is by far the slower, the relaxation time for the conditions important for laser machining being of the order of 10^{-11} s [12]. Since the spike of time of laser output power is of the order of 10^{-6} s (Fig. 1), equilibrium conditions can be reached. Therefore, these spikes can be considered as a continuous output from the laser and the absorption process can be described by the Lambert's law. If the laser output power intensity is considered as Gaussian, the spatial distribution of power intensity at the workpiece would also be Gaussian, i.e.

$$I(r,t) = (1-R_f)I_0(t)\exp[-(r/R)^2] \quad (1)$$

where I_0 is the power intensity absorbed at the surface and R_f is the surface reflectivity. The laser output power intensity is also time-dependent, therefore, the time-dependent pulse profile is considered to resemble the actual laser pulse shown in Fig. 1, and this profile is introduced in the numerical computation (Fig. 2). It should be noted here that the total energy content of the actual laser pulse is measured and then adopted to the theoretical profile, provided both pulse profiles have the same energy content.

Laser beam energy arriving at the workpiece surface is transferred into the bulk of the substance by conduction. In formulating the problem, radial symmetry is assumed, together with an incompressible and inviscid molten substrate ejected from the irradiated spot as the surface reaches at elevated temperature. The thermal properties of the workpiece are considered as being the temperature dependent, therefore, polynomial equations are developed, using the existing data in the literature [13], and employed in the solution of the problem. The energy dissipated with in the substrate and the momentum and continuity equations for the flow of molten material can be described as follows:

energy equation

$$\frac{\partial}{\partial z}\left(k\frac{\partial T}{\partial z}\right)+\frac{\partial}{\partial r}\left(k\frac{\partial T}{\partial r}\right)+\frac{k}{r}\left(\frac{\partial T}{\partial r}\right) + I_0(r,t)\exp[-\delta(z-z_0)] + \rho C_p V_r\frac{\partial T}{\partial r}-\frac{\partial}{\partial z}(\rho C_p V_z T)=\rho C_p\frac{\partial T}{\partial t} \quad (2)$$

continuity equation

$$\frac{\partial V_z}{\partial z}+\frac{1}{r}\frac{\partial}{\partial R}(rV_r)=0 \quad (3)$$

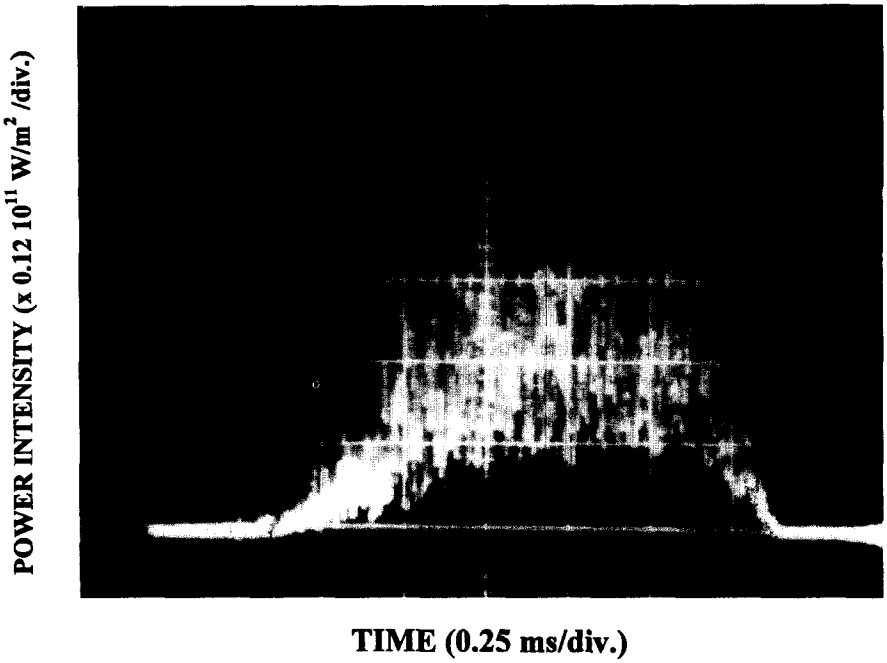

Fig. 1. Actual laser pulse.

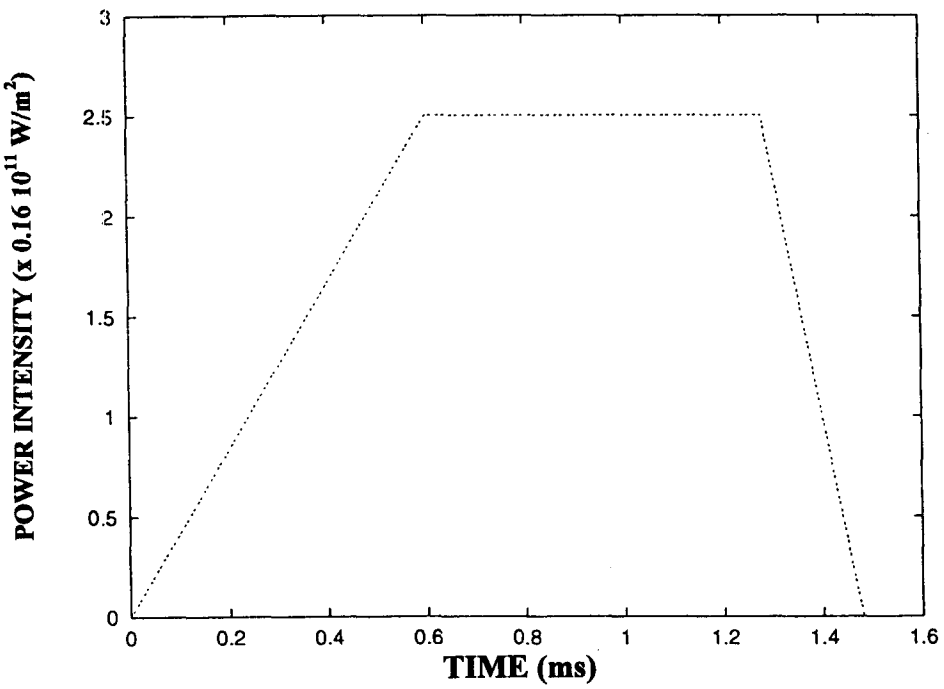

Fig. 2. Laser pulse used in computation.

momentum equations

$$\rho\left(V_r\frac{\partial V_z}{\partial r}+V_z\frac{\partial V_z}{\partial z}+\frac{\partial V_z}{\partial t}\right)=-\frac{\partial P}{\partial z}$$

$$\rho\left(V_r\frac{\partial V_r}{\partial r}+V_z\frac{\partial V_r}{\partial z}+\frac{\partial V_r}{\partial t}\right)=-\frac{\partial P}{\partial r}. \qquad (4)$$

The last two terms in energy equation allow for convection by the molten material ejected radially and axially, and it is subject to the boundary conditions:

$$\frac{\partial T}{\partial r}=0 \quad \text{at} \quad r=0$$

$$T=T_i \quad \text{at} \quad r=\infty$$

$$\left[\left(\frac{\partial T}{\partial s}\right)_{s=0}\right]_{liq}=\left(\frac{\rho VL}{k}\right)_{liq}$$

$$T = T_i \quad \text{at} \quad z = \infty$$

$$T = T_i \quad \text{at} \quad t = 0. \tag{5}$$

Evaporation of the surface may be expressed as follows: the liquid surface layer formed during a laser pulse moves into the metal at a rate determined by the quantity of vapor expelled. As the temperature of the liquid molecules is increased so the additional energy needed to free them from the binding forces decreases. The latent heat of vaporization, therefore, decreases with the temperature until the critical temperature is reached. The latent heat of evaporation can be written in terms of the surface temperature as [14]:

$$L(T) = L_0\left[1-\left(\frac{T_s}{T_c}\right)^2\right]^{1/2} \tag{6}$$

where L_0 is the latent heat of evaporation at absolute zero. The evaporating surface velocity can be obtained from the kinetic theory and the derivation of evaporating surface velocity is given in the Appendix. Therefore, it may be written as:

$$V_s = \left(\frac{K_B T}{2\pi m}\right)^{1/2} \exp\left(-\frac{L(T)}{K_B T}\right) \tag{7}$$

where K_B is the Boltzmann's constant. The melting front velocity (recession velocity) may be written as [12]:

$$V_{liq} = \frac{I_0}{\rho(L+C_p T_s)} \tag{8}$$

where T_s is the surface temperature.

The remaining boundary conditions for the continuity and momentum equations are:

$$V_r = 0 \quad \text{at} \quad r = 0$$

$$V_r = 0 \quad \text{at} \quad t = 0$$

$$\frac{\partial V_z}{\partial r} = 0 \quad \text{at} \quad r = 0$$

$$\frac{\partial V_z}{\partial r} = 0 \quad \text{at} \quad t = 0$$

$$\frac{P_z}{\rho^y} + \frac{V_z^2}{2} = \frac{P_s}{\rho^y} + \frac{V_s^2}{2} \quad \text{at normal to surface.}$$

An attempt to introduce a stream function into equations (3)–(5) to produce second-order equations leads a pair of highly non-linear equations. This method is, therefore, abandoned. The approach is to use a numerical scheme, which retains the cylindrical coordinate system and employs the axial distance from the original surface of the workpiece. A schematic view of the meshes used in the analysis is shown in Fig. 3. The energy equation is considered separately from the continuity and momentum equations, information on velocities from the latter being fed back into the convection terms, while the liquid surface temperatures determined from the energy equation defined the velocity boundary condition (equation (8)). Equations (3)–(5) can be rearranged as follows:

$$\frac{\partial V_z}{\partial t} = -V_r\frac{\partial V_z}{\partial r} - V_z\frac{\partial V_z}{\partial z} - \frac{1}{\rho}\frac{\partial P}{\partial z} = f(V_z,V_r,P,r,z,t) \tag{9}$$

$$\frac{\partial V_r}{\partial r} = \frac{\partial V_z}{\partial z} - \frac{V_r}{r} = g(V_z,V_r,r,z) \tag{10}$$

$$\frac{\partial P}{\partial z} = -\rho\left(V_r\frac{\partial V_r}{\partial r} + V_z\frac{\partial V_r}{\partial z} + \frac{\partial V_r}{\partial t}\right) = h(V_z,V_r,r,z,t). \tag{11}$$

Although equations (9)–(11) are simultaneous, they cannot be solved easily, therefore, a pressure correction term is introduced [15]. Let a tentatively calculated velocity field based on a guessed pressure field P^* is denoted by velocities u'_ζ, u'_η. Let the correct pressure P is obtained from:

$$P = P^* + P'. \tag{12}$$

The corresponding correction in the velocities u'_ζ, u'_η can be introduced in a similar manner, i.e.

$$u_\zeta = u^*_\zeta + u'_\zeta$$

$$u_\eta = u^*_\eta + u'_\eta. \tag{13}$$

The velocity correction formula for east face of the mesh element is given by [15]:

$$u_\zeta = u^*_\zeta + \frac{\Delta\eta}{A_e}\Delta P' \tag{14}$$

where $\Delta P'$ is the pressure difference across the mesh surface and A_e is the surface area of the east face of the mesh.

The important steps to compute the flow properties are; guess the pressure field; solve the momentum equations to obtain u'_ζ, u'_η; solve the pressure correction equation; calculate pressure by adding P' to P^*; set the correct pressure as a new guessed pressure P^*. Return to step 2 and repeat the whole procedure until the converged solution is obtained.

The governing equations (energy, momentum and continuity) in discretized form are given in the Appendix. A computer program is developed to solve the discretized equations with appropriate boundary conditions. The stability criterion for the numerical scheme in the general case is:

$$\Delta t \geqslant \rho^t_{M,N} C^t_{pM,N}\left\{k^t_{M,N}\left[\frac{2}{(\Delta r)^2} + \frac{2}{(\Delta z)^2}\right]\right.$$

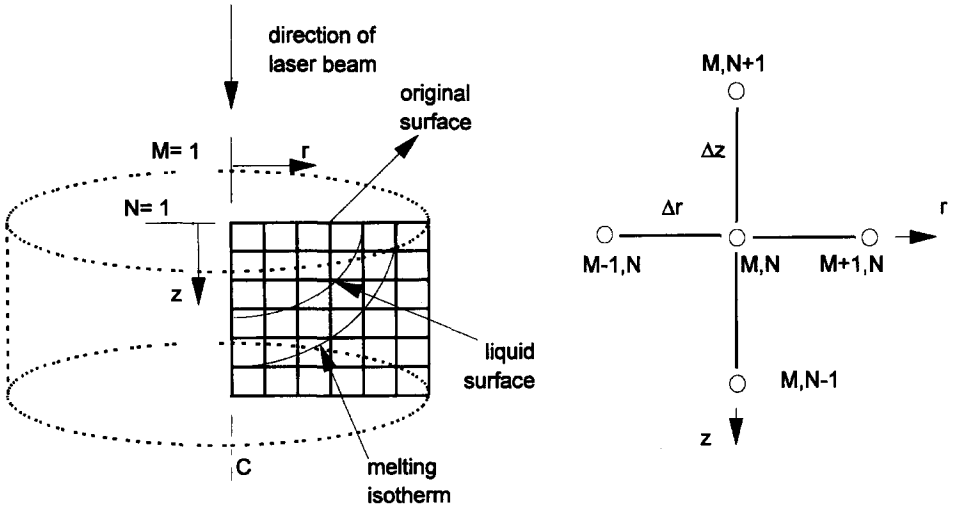

Fig. 3. A schematic view of the mesh used in the analysis.

$$+\rho^t_{M,N} C^t_{pM,N}\left[\frac{V^t_{r_{M+1,N}} - V^t_{r_{M-1,N}}}{2\Delta r} + \frac{V^t_{r_{M,N}}}{(M-1)\Delta r}\right.$$

$$\left. + \frac{V^t_{z_{M,N+1}} - V^t_{z_{M,N-1}}}{2\Delta z}\right] + \rho^t_{M,N}\left[C^t_{pM,N+1} - C^t_{pM,N-1}\right]$$

$$\times \frac{V^t_{r_{M,N}} + V^t_{z_{M,N}}}{2\Delta z} + C^t_{pM,N} V^t_{r_{M,N}} \frac{\rho^t_{M+1,N} - \rho^t_{M-1,N}}{2\Delta r}$$

$$\left. + C^t_{pM,N} V^t_{z_{M,N}} \frac{\rho^t_{M,N+1} - \rho^t_{M,N-1}}{2\Delta z}\right\}^{-1}.$$

This stability criterion is altered both at $r = 0$ and $z = 0$. The surface boundary condition is temperature dependent, which requires iteration, ensuring that the stability is satisfied along $r = 0$. Metals have value of absorption coefficient in the region of 10^8 m^{-1}, therefore, increments Δz and Δt in the program are taken as 0.25×10^{-8} m and 10^{-14} s, respectively, satisfying the stability criterion.

In solving the governing equations, thermal properties are considered as temperature dependent and polynomial equations are employed for this purpose. Results are obtained for the temporally and radially dependent power intensity distribution on the surface of the material. The assumed Gaussian distribution has its $1/e$ points 240 μm out from the centerline.

EXPERIMENTAL

The experimental set up is shown in Fig. 4. The experiment consisted of two parts. In the first part evaporated surface velocities were monitored and measured using a streak photography technique while in the second part surface temperature was measured using an optical method. An Nd YAG laser delivering output energy of 15–30 J at 1.2–2.7 ms pulses was employed to irradiate the stainless steel sheet at 1 mm thickness. The laser output energy and pulse length settings in the experiment were 21 J and 1.48 ms, respectively. A lens of 51 mm nominal focal length was used to focus the laser beam.

To monitor the evaporating surface velocity a high speed Strobodrum camera was used. This camera rotated a 1.5 m strip of 35 mm film at 3000 rpm reaching the film speed of 75 m s^{-1}. The camera was positioned so as to fill the width of the film with the event. The camera and laser was triggered from the same source. The velocity of the evaporated front was calculated by using the formula [16]:

$$\text{Velocity} = 156 \cdot \tan\theta$$

where θ is the angle between the free surface of the workpiece and the plane in which the particle travels through.

The principle of the temperature measurement is that, for a given temperature, there is a unique ratio of monochromatic emissive power intensities corresponding to two spectral frequencies. Therefore, knowing the emissive power ratio, the corresponding temperature can be calculated. The temporal distribution can be determined knowing that time dependent emissive power ratios correspond to two spectral frequencies. In the present experiment, the emissive power ratios were sampled at 5 μs intervals, since the time required for the surface evaporation of the workpiece was of the order of 50 μs. The measurement was carried out in the visible spectrum rather than in the infrared region. This is mainly because of the following reasons:

(i) Photodetector selection—a fast response time and high detectivity was required, since the rise time of the surface temperature was high and the power detected by a detector due to thermal radiation from the heated spot, which was less than 1 mm in diameter, was considerably small, i.e. of the order of 10^{-10} W m^{-1} at 1000 K at 6348 Å wavelength. The infrared

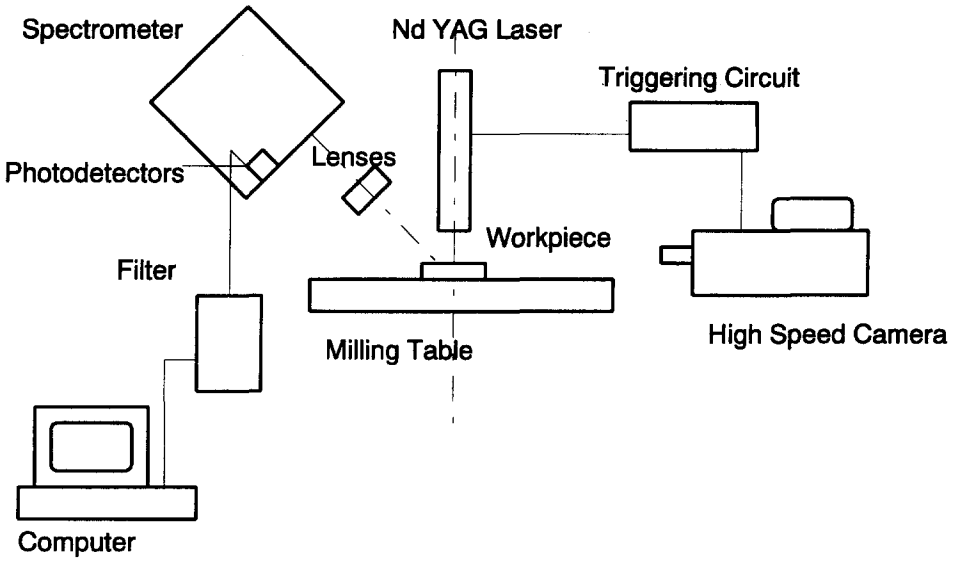

Fig. 4. Experimental set up.

detectors were limited in time of response for a spectral power detection, therefore, the photodetectors operating in the visible spectrum were considered.

(ii) This refers to the selection of the central frequencies. The emissive spectral power corresponding to gray body was high at long wavelengths, but the corresponding signal-to-noise ratio was poor and small changes in the emissive power ratios with temperature were obtained [17]. Alternatively, at small wavelengths the signal-to-noise ratio and emissive power ratios were high, but emissive power was considerably small, which was difficult to detect with any accuracy [17]. Consequently, three central wavelengths giving the optimum condition for the measurement were selected. These included 6348, 8000 and 10 000 Å.

The spectral analysis of the light emitted from the heated spot was performed using a grating spectrometer. Two photodetectors (RCA 80818) were spaced 2 mm apart at the exit slit of the spectrometer to detect the emitted light from the irradiated spot. This spacing corresponds to 164 Å spectral width. To integrate the monochromatic emissive power intensities seen by the photodetector, a 5.62 Å spectral bandwidth was considered. This corresponded to the spacing of the active area diameter of the photodetector. The spectrometer was positioned at 45° to the incident laser beam. Power emitted from the irradiated spot was focused onto the inlet slit of the spectrometer. To achieve this, two f6.3 lenses transmitting in the range of 0.28–1.7 μm were used. They were arranged close together, giving an effective focal length of 55 mm. The spectrometer slit width was selected as twice the image diameter of the irradiated spot at the inlet slit, which was of the order of 1 mm [17]. The further details of this measurement are not given here due to lack of space, but they are referred to in Ref. [17]. The error related to the present experiment was estimated as 7%.

RESULTS AND DISCUSSION

A schematic of a streak photograph is shown in Fig. 5. Several separate phases of the process are evident. Initially vapor is ejected from the cavity and decelerates rapidly as it expands, and a vapor front appears in highly luminous flares. On the workpiece surface, these appear as series of small spikes which initially appear to be about 10 μs apart, but after about 300 μs from the start of the laser pulse they fall off considerably in frequency. These correspond to ejection of some quantities of either vapor or liquid metal, i.e. these regions possibly correspond to intense and rapidly expanding plasma which is produced only when the cavity is shallow, at which time the power intensity is still high [18]. Consequently, evaporating surface velocities resulting after 300 μs may consist of the mixture of the liquid and vapor phases, therefore it becomes very difficult to measure the evaporating surface velocity with any accuracy after this interaction time.

Figures 6 and 7 show the radial variation of surface temperature for the peak laser power intensities of 0.4×10^{11} and 0.6×10^{12} W m^{-2} as time variable. The higher power intensities produce higher surface temperatures and a shorter time to reach the steady temperature plateau. The temperatures in excess of the melting point are reached at the radius corresponding to the $1/e$ points of the power intensity distribution and the major portion of the evaporation occurs within a region bounded by the $1/e$ points of the power intensity distribution. It is also evident that the radial temperature gradient (dT/dr) decays sharply after the point of $1/e$ points of the laser power intensity. This

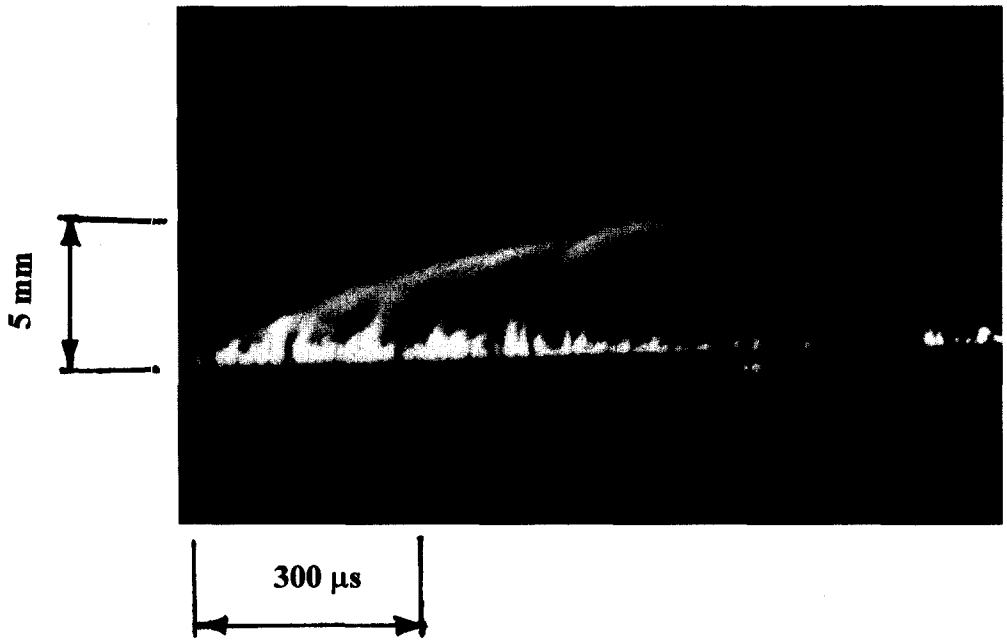

Fig. 5. Streak through photograph for steel workpiece.

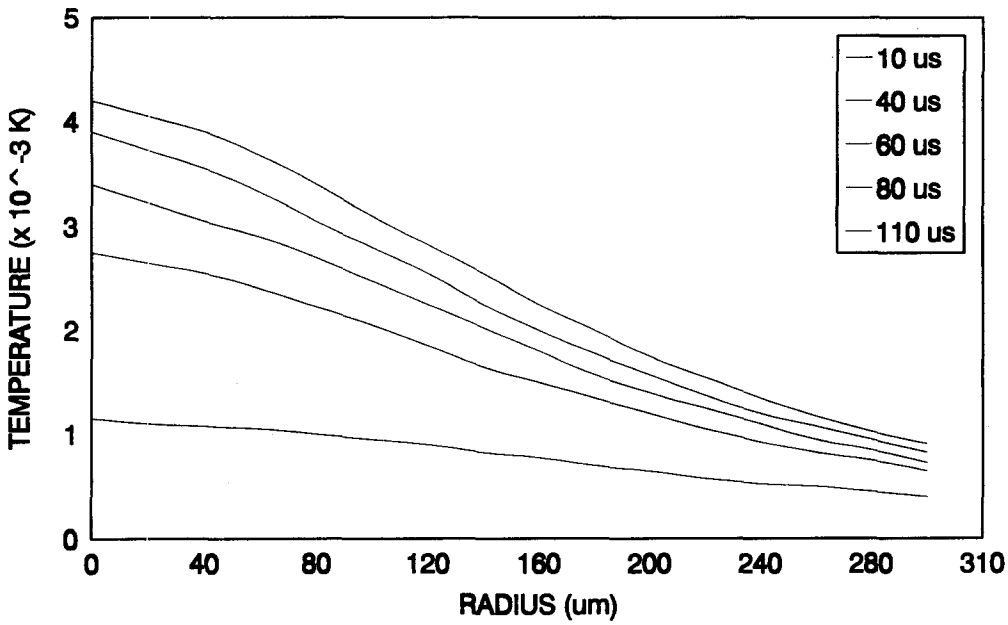

Fig. 6. Radial variation of surface temperature at different time intervals for laser peak power intensity of 0.4×10^{11} W m^{-2}.

may indicate that, in the initial part of the laser pulse, the energy gain by the substance through absorption is considerably higher as compared with the losses due to the radial effect of heat conduction. The flat top (plateau) of the temperature occurring within $1/e$ points of the laser power intensity is the result of phase change process. It should be noted here that the radial variation of pressure may result in some changes in thermodynamic equilibrium properties, which in turn modify the flat top to slight curvature.

Figure 8 shows the temporal variation of the surface temperature corresponding to the centerline of the laser power intensity with experimental results obtained for power intensities of 0.4×10^{11} and 0.6×10^{11} W m^{-2}. The rise time of the surface temperature to reach the melting point is considerably short in the case of power intensity 0.6×10^{11} W m^{-2}. When comparing the theoretical predictions with the experimental results, it is evident that both results are in good agreement up to the temperatures of 1600 K and some discrepancies between both results occur beyond this point. This may be due to one or all of

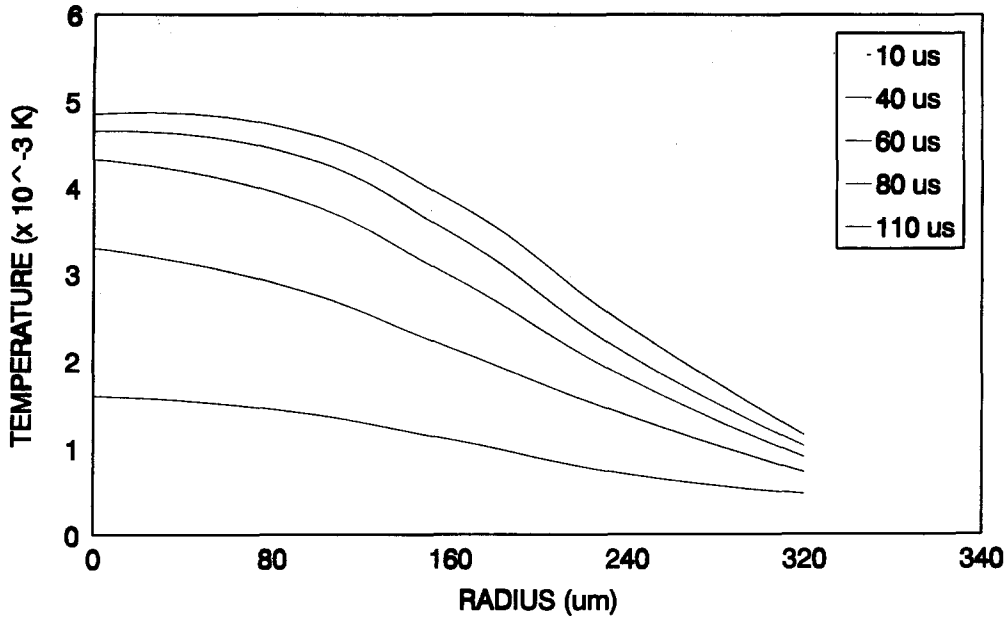

Fig. 7. Radial variation of surface temperature at different time intervals for laser peak power intensity of 0.6×10^{11} W m^{-2}.

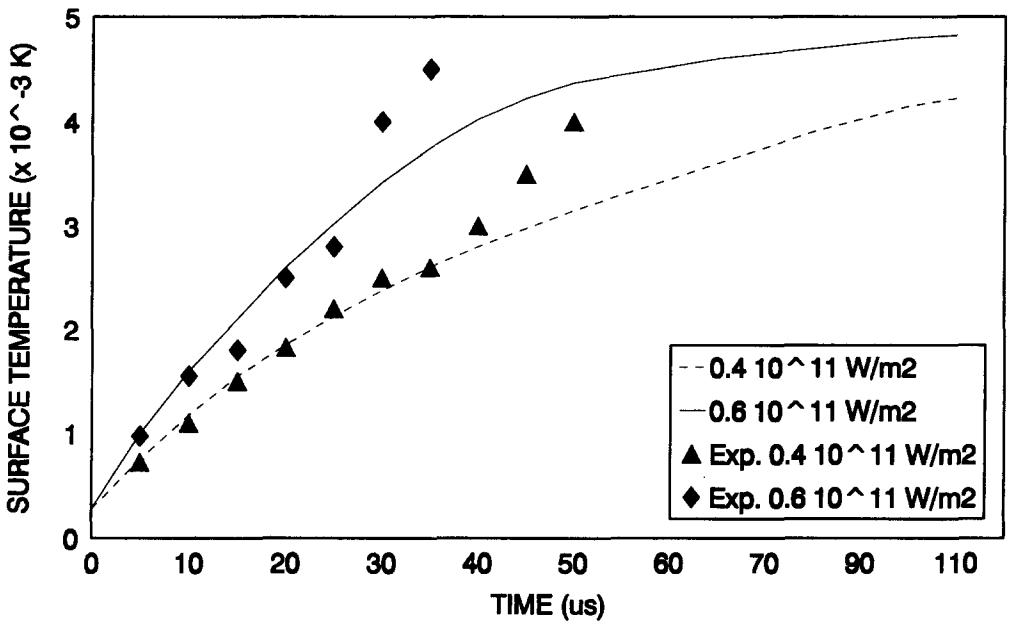

Fig. 8. Temporal variation of centerline surface temperature predicted and measured at two power intensities.

the following factors: (i) the assumptions made in the theoretical model, i.e. the flow of molten material is considered as incompressible and inviscid, which affects the surface temperature rise after the start of the evaporation process; (ii) the measurement error increases as the temperature increases, since the emissive power ratios corresponding to high temperatures fall close to unity [17], which may be difficult to detect with sufficient accuracy.

The growth of the temperature profiles inside the material along the centerline of the laser power intensity is shown in Figs. 9 and 10. It is evident that equation (5) permits only zero or positive temperature gradients at the surface. The apparent negative gradients occurring for 0.6×10 W m^{-2} power intensity is due to the fact that a zero gradient extends for too short a distance to be noticeable on the scale shown. The maximum temperature first occurs inside the material when surface temperatures reaches to about 4000 K. As time increases from here, the position of

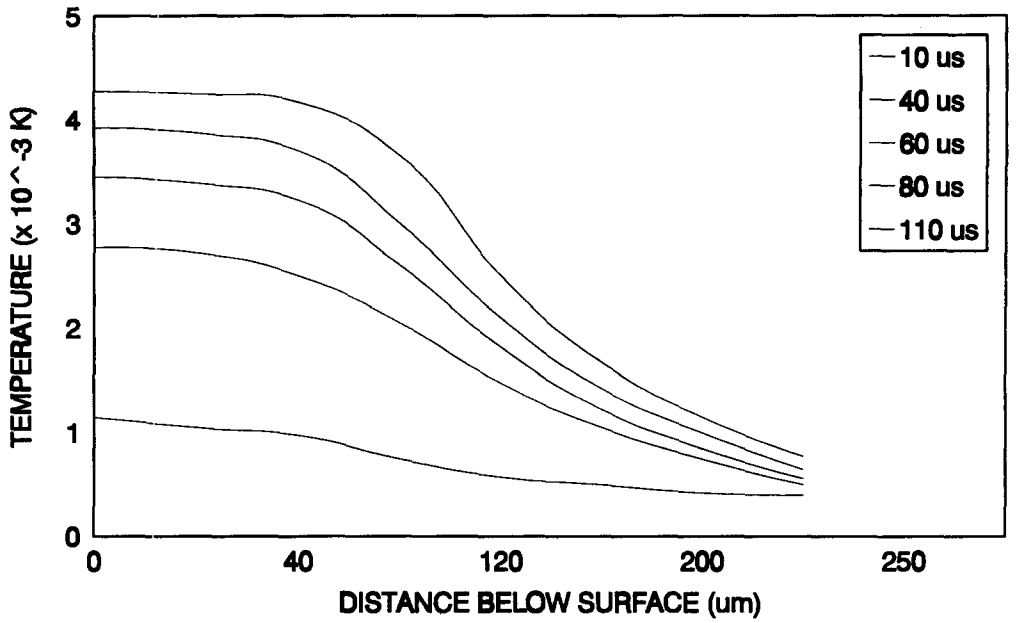

Fig. 9. Temperature profile inside the workpiece at different time intervals for laser peak power intensity of 0.4×10^{11} W m^{-2}.

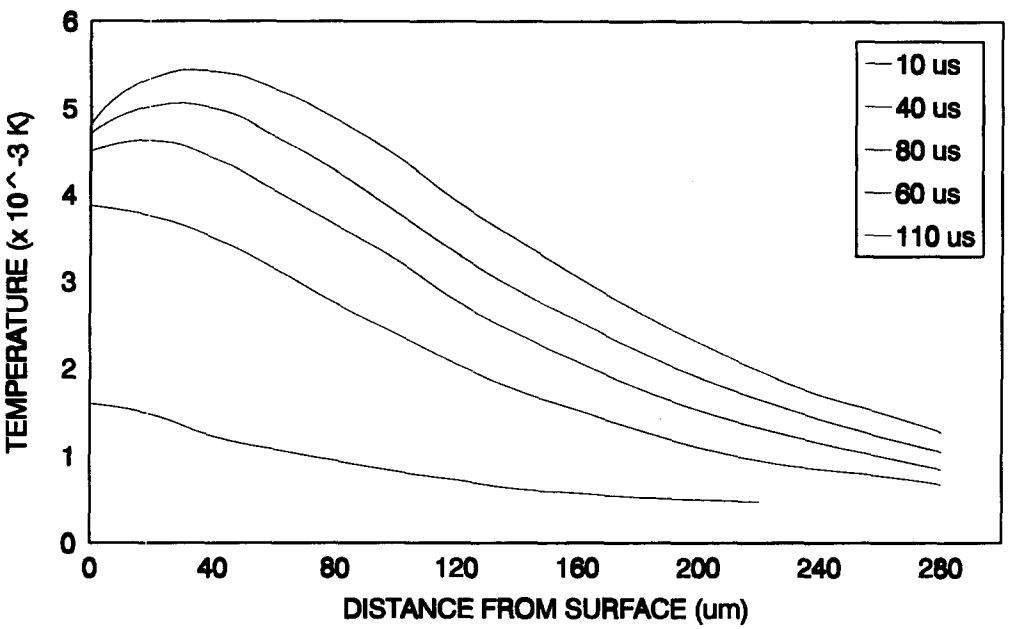

Fig. 10. Temperature profiles inside the workpiece at different time intervals for laser peak power intensity of 0.6×10^{11} W m^{-2}.

the point of maximum temperature progresses into the material, reaching a steady value at approximately 40 μm below the surface. The maximum temperature occurring below the surface suggests two possibilities for the material removal process. First, the nucleation rate will be sufficiently high, so that material may burst from the cavity, provided that the saturated vapor pressure in the nucleating region exceeds the surface pressure and the material is superheated, as confirmed by the previous study [19]. The second possibility is that when the laser power intensity is sufficiently high for the maximum temperature in the cavity to reach the critical point and become vapor, then an explosion can occur if the saturated vapor pressure at the critical temperature exceeds the pressure in the cavity. This process may occur for very high power intensities ($\sim 10^{13}$ W m^{-2}) [19].

Figures 11 and 12 show the radial variation of melting front velocities as time variable. The variation of melting front velocities is similar to the radial vari-

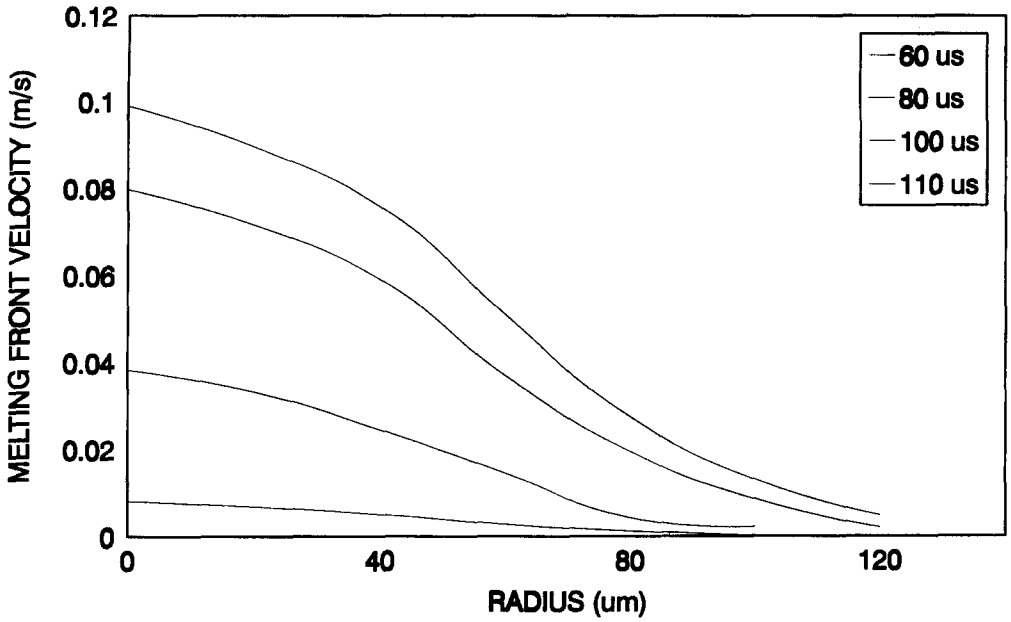

Fig. 11. Radial variation of melting front velocities at different time intervals for laser peak power intensity of 0.4×10^{11} W m^{-2}.

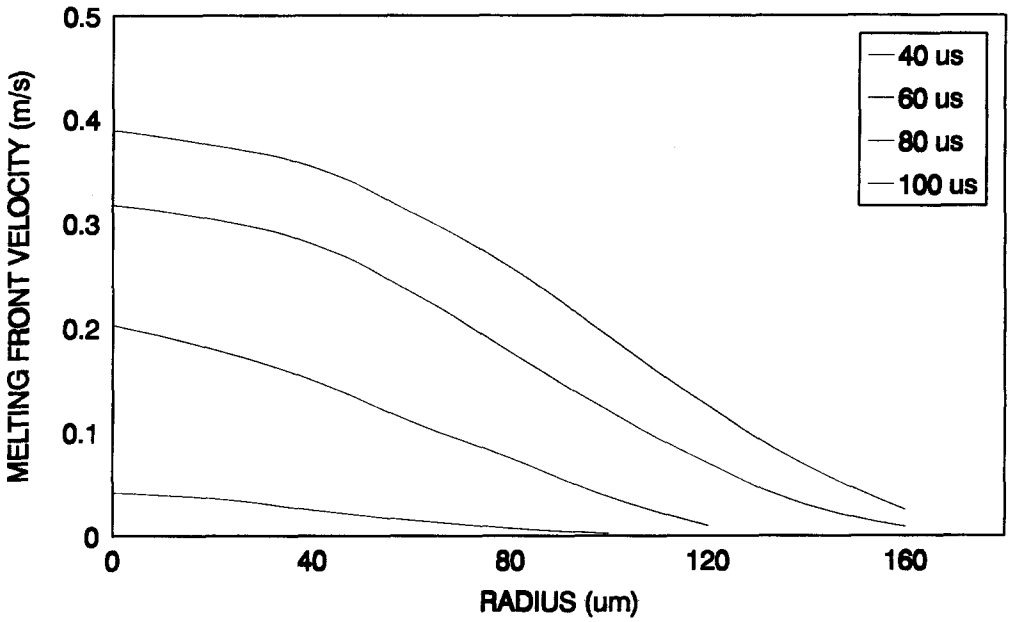

Fig. 12. Radial variation of melting front velocities at different time intervals for laser peak power intensity of 0.6×10^{11} W m^{-2}.

ation of surface temperatures providing that they reach maximum at the centerline and become minimum at $1/e$ points of the laser power intensity. The melting front velocities corresponding to 0.6×10^{11} W m^{-2} power intensity are almost of the order of four times higher than that corresponding to 0.4×10^{11} W m^{-2} power intensity. This may suggest that 65% increase in power intensity results in substantial increase in melting front velocities, which in turn enhances the penetration speed of the workpiece. It should be noted here that this argument can only be true for the machining power intensities considered in the present study.

Figure 13 shows the temporal variation of evaporating surface velocities predicted from the present model and obtained from the experiment. When comparing the theoretical predictions with the experimental results, it is evident that both results are in good agreement. Once the evaporation process is fully developed, evaporating front velocity remains almost

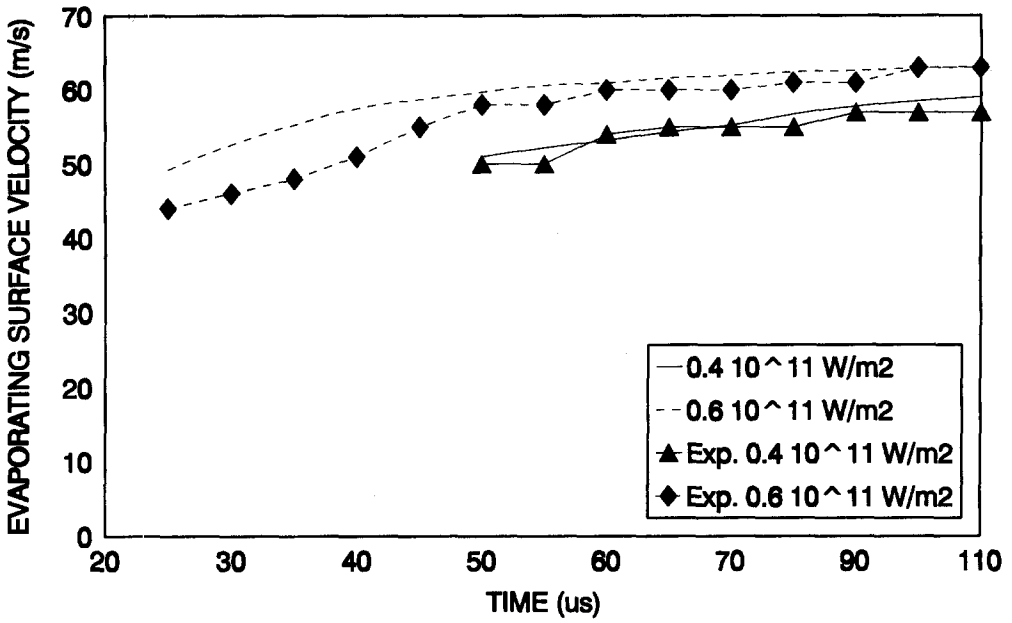

Fig. 13. Temporal variation of evaporating surface velocities predicted and measured at two peak power intensities.

constant with time. This may be due to energy balance attained at the workpiece surface, in this case, the energy gained by the material through the absorption is balanced by the energy dissipated due to convection and conduction. The discrepancies occurring between both results may be due to the measurement errors and/or assumptions made in the theoretical model.

CONCLUSIONS

A theoretical model governing laser–workpiece interaction employing conduction, phase change, convection processes and mass removal mechanism is presented, and the results are discussed. Liquid and vapor expulsion due to pressure gradient at the surface are considered. A numerical approach is introduced to solve energy, momentum and continuity equations. The results are given for the temporally and radially dependent power intensity distribution of $1/e$ points corresponding to 240 μm out from the centerline. The conclusions derived from the present study may be listed as follows.

(1) In the initial part of the laser heating pulse, vapor ejection from the irradiate spot is evident and it appears in highly luminous flares of 10 μs apart. However, intense and rapidly expanding plasma occurs after 300 μs of the interaction time, therefore, it becomes difficult to measure the evaporating front velocity with any accuracy after this interaction time.

(2) The temperatures in excess of the melting point are reached when the radius corresponds to $1/e$ points of the laser intensity distribution and evaporation mainly occurs within this region. Rapid decay in radial temperature gradient occurring just after $1/e$ points of the laser power intensity distribution suggests that the energy gain by the substance through the absorption process is considerably high as compared with the losses due to radial effect of heat conduction.

(3) The surface temperatures predicted are in good agreement with the experimental results up to temperatures of 1600 K. The discrepancies between both results occurring at elevated temperatures are due to the assumptions made in the analysis and/or measurement errors as a result of emissive power ratios, since they fall to unity at high temperatures.

(4) The maximum temperature lies below the surface at high laser power intensities and this suggests that the mass removal mechanism is governed by the burst of liquid from the cavity and/or explosion of the vapor bubbles formed in the liquid phase.

(5) The melting front velocity increases considerably with increasing laser power intensity. This indicates that some increase in power intensity enhances the penetration speed of the workpiece substantially.

(6) Evaporating front velocities predicted agree well with the experimental results. Once the evaporation process is fully developed, evaporating front velocity remains almost constant with time, which shows the attainment of the energy balance at the surface.

REFERENCES

1. M. Tsai and C. Weng, Linear stability analysis of molten flow in laser cutting, *J. Phys. D Appl. Phys.* **26,** 719–727 (1993).
2. B. S. Yilbas, Analytical solution for heat conduction mechanism appropriate to the laser heating process, *Int. Commun. Heat Mass Transfer* **20,** 545–555 (1993).

3. A. F. A. Hoadley, M. Rappaz and M. Zimmermann, ξHeat-flow simulation of laser remelting with experimental validation, *Metall. Trans. B* **22B,** 101–109 (1991).
4. W. Schulz, D. Becker, J. Franke, R. Kemmerling and G. Herziger, Heat conduction losses in laser cutting of metals, *J. Phys. D Appl. Phys.* **26,** 1357–1363 (1993).
5. G. Simon, U. Gratzke and J. Kroos, Analysis of heat conduction in deep penetration welding with a time-modulated laser pulse, *J. Phys. D Appl. Phys.* **26,** 862–869 (1993).
6. O. O. Diniz Neto and C. A. S. Lima, Nonlinear three-dimensional temperature profiles in pulsed laser heated solids, *J. Phys. D Appl. Phys.* **27,** 1795–1804 (1994).
7. B. F. Blackwell, Temperature profile in semi-infinite body with exponential source and convective boundary conditions, *ASME J. Heat Transfer* **112,** 567–571 (1990).
8. W. W. Duley, *Laser Processing and Analysis of Materials*, 1st Edn, p. 101. Plenum Press, New York (1983).
9. B. S. Yilbas, A. Sahin and R. Davies, Laser heating mechanism including evaporation process initiating laser drilling, *Int. J. Mach. Tools Manufact.* **35,** 1047–1062 (1995).
10. B. S. Yilbas and A. Sahin, Laser heating mechanism including evaporation process, *Int. Commun. Heat Mass Transfer* **12,** 509–518 (1994).
11. B. S. Yilbas, Heating of metals at a free surface by laser irradiation an electron kinetic theory approach, *Int. J. Engng Sci.* **24,** 1325–1334 (1986).
12. B. S. Yilbas and A. Sahin, Heating mechanism in relation to the laser machining process, *Pram. J. Phys.* **41,** 453–465 (1993).
13. W. W. Duley, *Laser Processing and Analysis of Materials*, 1st Edn, p. 86. Plenum Press, New York (1983).
14. B. S. Yilbas and K. Apalak, The basic concepts of heat transfer mechanisms during laser drilling of metals, *Egypt J. Phys.* **18,** 133–156 (1987).
15. S. V. Patankar, *Numerical Heat Transfer and Fluid Flow*, 1st Edn, p. 126. Series in Computational Methods in Mechanics and Thermal Sciences, McGraw-Hill, New York (1980).
16. B. S. Yilbas, The study of laser produced plasma behavior using streak photography, *Jap. J. appl. Phys.* **24,** 1417–1420 (1985).
17. B. S. Yilbas, Optical method for measurement of the temporal variation of temperature at the surface of a metal heated by a laser, *Int. J. Opt.* **15,** 108–116 (1986).
18. K. Danisman, B. S. Yilbas and Z. Yilbas, Study of some characteristics of plasma generated during a CO_2 laser cutting process, *Opt. Laser Technol.* **24,** 33–38 (1992).
19. B. S. Yilbas, R. Davies and Z. Yilbas, Surface line and plug flow models governing laser produced vapor from metallic surfaces, *Pram. J. Phys.* **38,** 195–209 (1992).
20. D. Tabor, *Gases, Liquids and Solids and Other States of Matter*, 3rd Edn, p. 272. Cambridge University Press, Cambridge (1991).

APPENDIX: DERIVATION OF EVAPORATING SURFACE VELOCITY.

The rate of change of latent heat with temperature can be expressed as;

$$\frac{dL}{dT} = \frac{L}{T} + (C_{pv} - C_{pl}) - \frac{L}{v_v - v_l}\left[\left(\frac{\partial v_v}{\partial T}\right)_P - \left(\frac{\partial v_l}{\partial T}\right)_P\right]$$

where C_{pv} and C_{pl} are specific heats at constant pressure for vapor and liquid states, respectively, and v_v and v_l are specific volumes for vapor and liquid states. Although integration of the latent heat over the temperature 0–T_c is impossible, it can be used to show that little inaccuracy is involved in taking the room temperature latent heat as the latent heat at absolute zero. By putting:

$$v_v \gg v_l \quad \text{and} \quad \left(\frac{\partial v_v}{\partial T}\right)_P \gg \left(\frac{\partial v_l}{\partial T}\right)_P$$

i.e. the specific volume of gas is much greater than the condensed liquid and its rate of change with temperature at constant pressure is correspondingly greater. Therefore,

$$v_v = \frac{ZRT}{P} \quad \text{or} \quad \frac{\partial v_v}{\partial T} = \frac{ZR}{P}$$

then it yields:

$$\frac{dL}{dT} = \frac{L}{T} + (C_{pv} - C_{pl}) - \frac{L}{T} = \Delta C_p.$$

ΔC_p is extremely small for temperatures up to room temperature and so little error will result in taking L_0 as the latent heat at room temperature.

According to Maxwell's law the velocity distribution of molecules may be written as [20]:

$$f(V_z)dV_z = \left(\frac{m}{2\pi K_B T}\right)^{1/2} \exp\left(-\frac{mV_z^2}{2K_B T}\right)dV_z,$$

where V_z, T, K_B and m are the velocity in the direction normal to the surface, temperature, Boltzmann's constant and mass of the atom, respectively. The function $f(V_z)dz$ is also:

$$f(V_z)dV_z = \frac{\text{Number of atoms with velocity } V_z \text{ to } V_z + dV_z \text{ per unit volume}}{\text{Number of atoms per unit volume}}.$$

Only those molecules whose velocity is greater than is given by [20]:

$$\frac{1}{2}mV_{min}^2 = L(T),$$

where V_{min} lies in the z direction, will escape from the retaining potential. If n is the number of atoms per unit volume then the number of atoms with velocities V_z to $V_z + dV_z$ per unit volume is:

$$nf(V_z)dV_z$$

and the number of atoms with these velocities passing a unit area per unit time is

$$nf(V_z)V_z dV_z.$$

All the atoms for which $V_z > V_{min}$ do not return to their equilibrium position and are evaporated. If G is the number of atoms evaporated per unit time per unit area, then:

$$G = \int_{V_{min}}^{\infty} nf(V_z)V_z dV_z$$

$$= n\left(\frac{K_B T}{2\pi m}\right)^{1/2} \int_{V_{min}}^{\infty} \exp\left(-\frac{mV_z^2}{2K_B T}\right)V_z dV_z$$

or

$$G = n\left(\frac{K_B T}{2\pi m}\right)^{1/2} \exp\left(-\frac{L(T)}{K_B T}\right).$$

If atoms are equally spaced within the lattice a surface layer would consist of $n^{2/3}$ with an evaporation time $n^{2/3}G$. The average velocity of the surface (V_s) is therefore:

$$V_s = \frac{1}{n^{1/3}} \frac{G}{n^{2/3}}$$

or

$$V_s = \left(\frac{K_B T}{2\pi}\right)^{1/2} \exp\left(-\frac{L(T)}{K_B T}\right).$$

Discretized equations

The energy equation may be discretized using finite difference scheme and this may be written as (for the general case):

$$T^{t+1}_{M,N} = T^t_{M,N}\left\{-\frac{\Delta t}{\rho^t_{M,N}} K^t_{M,N}\left(\frac{2}{(\Delta r)^2}+\frac{2}{(\Delta z)^2}\right)\right.$$

$$\times \rho^t_{M,N} C^t_{pM,N}\left(\frac{V^t_{rM+1,N}+V^t_{rM-1,N}}{2\Delta r}\right.$$

$$\left.+\frac{V^t_{rM,N}}{(M-1)\Delta r}+\frac{V^t_{zM,N+1}-V^t_{zM,N-1}}{2\Delta z}\right)$$

$$+\rho^t_{M,N}(C^t_{pM,N+1}-C^{tM}_{pM,N-1})\frac{V^t_{rM,N}+V^t_{zM,N}}{2\Delta r}$$

$$+C^t_{rM,N} V^t_{rM,N}\frac{\rho^t_{M+1,N}\rho^t_{M-1,N}}{2\Delta r}$$

$$\left.+C^t_{pM,N} V^t_{zM,N}\frac{\rho^t_{M,N+1}\rho^t_{M,N-1}}{2\Delta z}\right\}$$

$$+\frac{\Delta t T^t_{M,N+1}}{\rho^t_{M,N} C^t_{PM,N}}\left(\frac{k^t_{M,N}}{(\Delta z)^2}+\frac{k^t_{M,N+1}-k^t_{M,N-1}}{4(\Delta z)^2}\right.$$

$$\left.-\frac{\rho^t_{M,N} C^t_{p-M,N} V^t_{zM,N}}{2\Delta z}\right)+\frac{\Delta t T^t_{M,N-1}}{\rho^t_{M,N} C^t_{pM,N}}\left(\frac{k^t_{M,N}}{(\Delta z)^2}\right.$$

$$\left.-\frac{k^t_{M,N+1}-k^t_{M,N-1}}{4(\Delta z)^2}+\frac{\rho^t_{M,N} C^t_{pM,N} V^t_{zM,N}}{2\Delta z}\right)$$

$$+\frac{\Delta t T^t_{M+1,N}}{\rho^t_{M,N} C^t_{pM,N}}\left\{\frac{k^t_{M,N}}{(\Delta r)^2}\left[1+\frac{1}{2(M-1)}\right]\right.$$

$$\left.+\frac{k^t_{M+1,N}-k^t_{M-1,N}}{4(\Delta r)^2}+\frac{\rho^t_{M,N} C^t_{M,N} V^t_{rM,N}}{2\Delta r}\right\}$$

$$+\frac{\Delta t T^t_{M-1,N}}{\rho^t_{M,N} C^t_{pM,N}}\left\{\frac{k^t_{M,N}}{(\Delta r)^2}\left[1+\frac{1}{2(M-1)}\right]\right.$$

$$\left.-\frac{k^t_{M+1,N}-k^t_{M-1,N}}{4(\Delta r)^2}+\frac{\rho^t_{M,N} C^t_{M,N} V^t_{rM,N}}{2\Delta r}\right\}$$

$$+\frac{I^t_{0M}\,\delta \exp\left[-\delta(Z_n-Z_0)\right]\Delta t}{\rho^t_{M,N} C^t_{pM,N}}.$$

The functions f, g and h from equations (9)–(11) are determined after applying a finite difference scheme, and the following result in the general case:

$$f(V_z,V_r,P,r,t) = -\left[V^t_{zM,N}(V^t_{zM,N+1}-V^t_{zM,N-1})\right.$$

$$\left.+V^t_{rM,N}(V^t_{zM+1,N}-V^t_{zM-1,N})+\frac{P^t_{M,N+1}-P^t_{M,N-1}}{2\rho^t_{M,N\Delta z}}\right]$$

$$g(V_z,V_r,r,t) = -\left[\frac{V^{t+1}_{zM,N+1}-V^{t+1}_{zM,N-1}}{2\Delta z}+\frac{V^{t+1}_{rM,N}}{(M-1)\Delta r}\right]$$

and

$$h(V_z,V_r,r,z,t) = -\rho^{t+1}_{M,N}\left[V^{t+1}_{rM,N}\left(\frac{V^{t+1}_{rM+1,N}-V^{t+1}_{rM-1,N}}{2\Delta r}\right)\right.$$

$$\left.+V^{t+1}_{zM,N}\left(\frac{V^{t+1}_{zM,N+1}-V^{t+1}_{zM,N}}{2\Delta z}\right)+\frac{V^{t+1}_{rM,N}-V^{t+1}_{rM,N}}{\Delta t}\right].$$

At the boundaries, these equations are modified by the insertion of the boundary conditions.